OPTICS

Self-positioning microdevices enable adaptable spatial displaying

Qi Guo[1]†, Zeyi Li[1]†, Yajie Zhou[1], Shanshan Zhao[1], Yaxin Wang[1], Mingjiang Zhang[1], Guangen Li[1], Zhi Tong[1], Taotao Zhuang[1]*, Shu-Hong Yu[2,3]*

Adaptable display with spatial imaging, fostering advancements in extended reality with unconventional form requirements, is indispensable in scientific research, telemedicine, rescue, and space exploration. The adjustable photon spin angular momentum derived from chiral optical materials offer applicative lights for binocular stereo imaging displays, thus allowing an unimaginable immersive experience while maintaining awareness of surroundings. However, current chiral illuminant struggles to obtain adequate electroluminescence asymmetry during power-on display. Here, we present a designed self-positioning strategy to build new flexible spatial displays, integrating numerous multilayered circularly polarized electroluminescent microdevices, for real-time depth information control on the screen. With the devices' luminescence asymmetry value of up to 1.0 under electro-excitation, we visualize third-dimensional information using our chiral material-integrated tablet. Afterward, combined with a robot, we realize a series of remote human-machine interaction operations based on extended reality conditions. Our adaptable spatial display bridges the gap between virtuality and reality, making pioneering explorations in chiral luminous fields for extended reality and beyond.

INTRODUCTION

Displaying devices play an irreplaceable role in the information era (*1*–*3*), completing over 70% of information transmission in human-robot interaction (*4*–*6*), whether it is scientific instruments (*7*, *8*), industrial equipment (*9*, *10*), medical electronic apparatus (*11*, *12*), or spacecraft (*13*–*15*). However, most screens have long been limited to rigid structure and exhibiting two-dimensional (2D) images, lacking crucial applicability and depth details. Spatial displaying substantially enhances the image's content, boosts its realism, and facilitates its understanding, allowing real-time immersive human-robot interaction (Fig. 1A). In addition, a 3D displaying system that provides a more authentic perception and a user-friendly interface for human-robot interaction is sought after but still poses challenges. Circularly polarized light drives display come into sight, offering distinct rotated patterns to the observer's left and right eyes based on the difference in photon spin angular momentum and polarized glasses, thus creating stereoscopic imaging effects with minimal viewing angle restrictions and reduced dizziness (*16*–*18*).

Compared to complex physical-optics methods for generating circularly polarized light, chiral luminous materials, which are capable of circularly polarized luminescence (CPL), show the promise to be processed and integrated into modern adaptable spatial displaying electronics (*19*). However, current CPL-based display technology is limited to static stereoscopic imaging (*20*, *21*), since it is impossible to dynamically control the luminescence pixels in real-time on the basis of input digital signals. An adaptable spatial displaying panel that enables tunable and visible CPL when operating under current has not been achieved.

[1]Hefei National Research Center for Physical Sciences at the Microscale, Department of Chemistry, University of Science and Technology of China, Hefei 230026, PR China. [2]Department of Chemistry, New Cornerstone Science Institute, Institute of Biomimetic Materials and Chemistry, Anhui Engineering Laboratory of Biomimetic Materials, Division of Nanomaterials and Chemistry, Hefei National Research Center for Physical Sciences at the Microscale, University of Science and Technology of China, Hefei 230026 China. [3]Institute of Innovative Materials (I2M), Department of Materials Science and Engineering, Department of Chemistry, Southern University of Science and Technology, Shenzhen 518055, China.
*Corresponding author. Email: tzhuang@ustc.edu.cn (T.Z.); shyu@ustc.edu.cn (S.-H.Y.)
†These authors contributed equally to this work.

RESULTS

We took a view and manufactured the 3D display of which arrays of CPL generation units constitute the pixels (Fig. 1B). Each CPL unit presents as a microdevice with a multilayer structure split into an electroluminescent section and a circularly polarized segment, through the collaboration of diverse functional layers (Fig. 1, C and D).

For electrically excited illumination, we applied alternating current (AC) electric field to drive light-emitting components via spatial contacts between parallels and warps that permits high device stability and low processing complexity (*22*, *23*). Thereafter, we designed a self-positioning in situ polymerization strategy to build a multimicrosphere collaborative circular polarizer (MCCP) embedded with chiral liquid crystals (Fig. 2A), enabling the generated electroluminescence to be chiral (*24*–*26*). The multimicrosphere layer with appropriate thickness preserves the helical structure of chiral liquid crystals, allowing for the emergence of CPL with continuously adjustable wavelengths and large luminescence dissymmetry factors (g_{lum}), while offering the freestanding characteristic without encapsulation.

In our developed one-step synthesis of the MCCP, the chiral microspheres were formed by wrapping the hydrophobic end of polyvinyl alcohol (PVA) around chiral liquid crystals and well dispersed in the prepolymer solution of polyacrylamide (PAM). Uncured MCCP should spontaneously move from hydrophobic regions to hydrophilic luminescent locations, thanks to its fine hydrophilicity and fluidity derived from lowering effect of PAM on frictional resistance between liquids (Fig. 2B and fig. S1A). We further simulated the pressure distribution of the uncured MCCP on panel surface using the finite-element method (Fig. 2C and movie S1), which explained its self-positioning capacity (*27*) (Fig. 2D, fig. S1B, and movie S2), thus helping to downgrade the processing challenge (fig. S1, C to E).

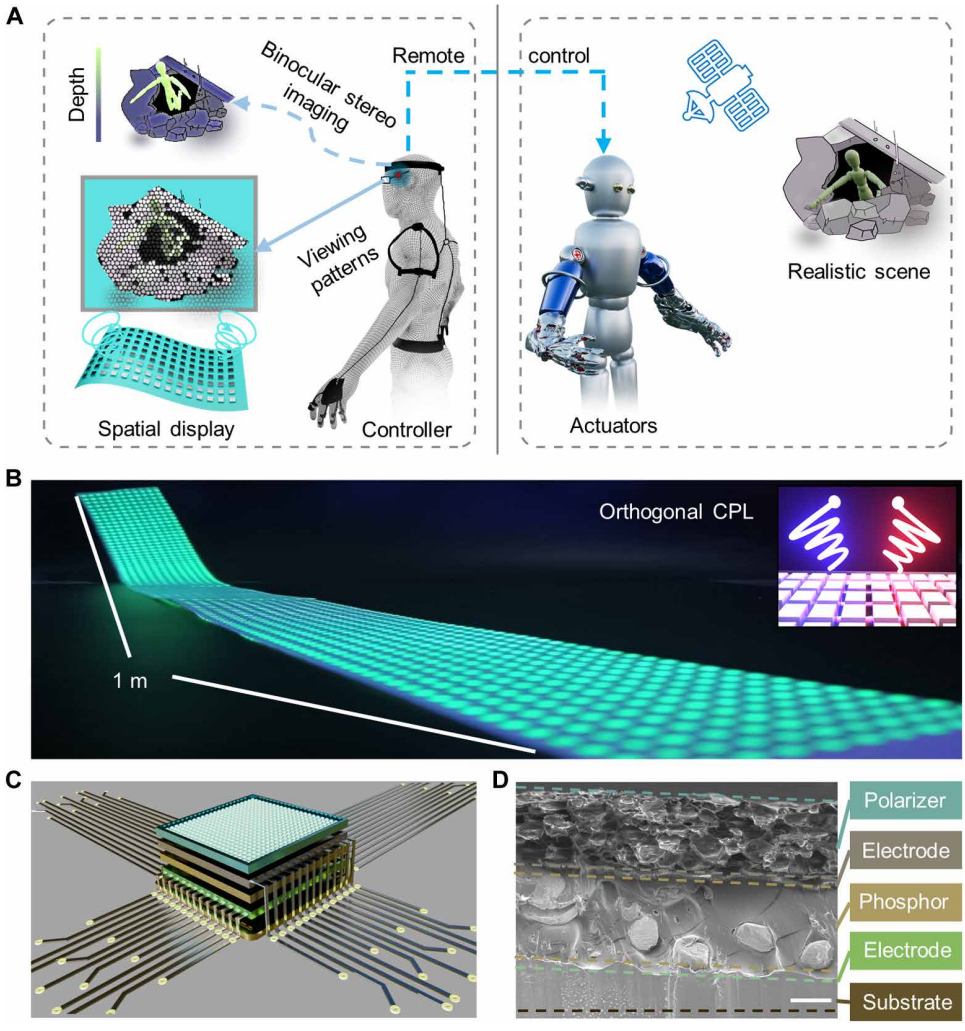

Fig. 1. Human-robot interaction enabled by spatial displays based on CPL. (**A**) Spatial display based on CPL achieves deep interaction with robot by providing depth information. (**B**) Schematic diagram and photo of the CPL-based adaptable spatial display. Size of display, 1 m × 0.12 m. (**C** and **D**) Structure design of the pixel (CPL-microdevice) of the CPL display (C), and the corresponding functional layer morphologies observed by cross-sectional SEM (D). Scale bar in (D), 20 μm.

After being self-positioning to desired positions, the prepolymer system (Fig. 2E) was gradually solidified into a uniform MCCP film with the assistance of ultraviolet (UV) light irradiation (figs. S2 and S3) and tightly bonded with the luminescent sections because of the strong adhesion of PAM. Densely packed microspheres (Fig. 2F) were observed in the MCCP film using cross-sectional scanning electron microscopy (SEM), allowing high-quality CPL production.

We then examined the chiroptical performance of the CPL generation device, to lay the foundation for the prospective stereoscopic display. The MCCP, consisting of chiral microspheres, selectively converted the electroluminescence of the photoelectric layer (fig. S4, A to C) to CPL with controlled handedness (Fig. 2G and fig. S4D), relying on the intrant chiral dopants. We tuned the component ratio, that is, the mass fraction of R/S5011 (chiral dopants) and nematic liquid crystals (E7) we used, of MCCP to align its photonic bandgap (PBG) with the electroluminescence spectrum of the phosphor (Fig. 2H and fig. S4, E to G), toward achieving highest luminescence asymmetry. We also studied the MCCP thickness dependence of the device performance and concluded that 30- to 40-μm MCCP layer thickness eventuated the strongest CPL signals (Fig. 2I) with the g_{lum} value up to 1.0 under power on (Fig. 2J).

We also used a fiber-coupled spectrometer to measure the intensity of the transmitted light passing through the orthogonal polarization plane without (Fig. 2K) and with (Fig. 2L) conversion by a quarter-wave plate (converting CPL into linear-polarized light), corroborating distinctly favorable circular polarization characteristics of the emissions from the multilayer device. We further evaluated the visualization of generated CPL using photoluminescence spectra analysis. The noticeable photoluminescence intensity variations under left- and right-handed circular polarized filters resulted from the passage of the synclastic handedness CPL while forbidding the opposite one (fig. S4H), which also manifested as a remarkable discrepancy in the luminance (fig. S4I), providing feasibility for stereo-displaying.

These gratifying results evidenced the high-quality electro-CPL generation, thereby allowing for the desired immersive visual perception. The neo-micro-CPL device we structured could be refined into the upper MCCP section and the thermoplastic polyurethanes dispersing ZnS phosphors layer, sandwiched between two poly(2,3-

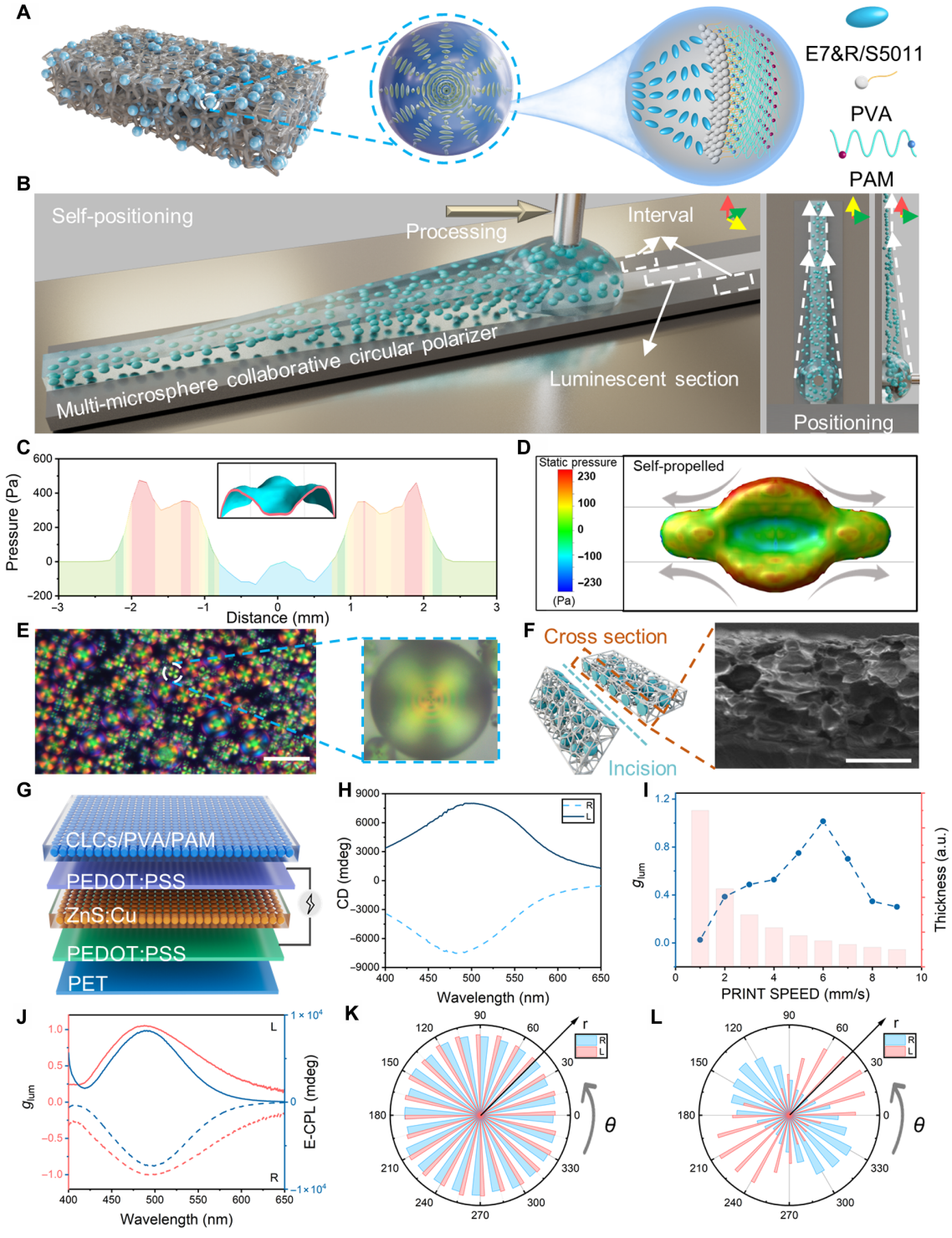

Fig. 2. Characterization of the MCCP and chiroptical performance of CPL devices. (**A**) Illustration of the structure of the multimicrosphere collaborative circular polarizer, with abundant chiral liquid crystal–composed microspheres (encapsulated by PVA), which were distributed in PAM. (**B**) Schematic diagram of self-positioning synthetic strategy. (**C**) Self-positioning process simulation at the hydrophilic-hydrophobic interface. (**D**) Simulation of the pressure distribution of uncured MCCP droplets on different zones of the panel surface. (**E**) Polarized optical microscopy (POM) image of uncured MCCP, showing the Maltese cross pattern with characteristic stripes. Scale bar, 20 μm. (**F**) SEM image of the cross section of MCCP, visualizing dissected chiral liquid crystal microspheres. Scale bar, 20 μm. (**G**) Schematic illustration of the designed layered device, generating both left- and right-handed CPL. (**H**) Circular dichroism spectra of the MCCP. (**I**) The luminescence dissymmetry factor spectra changed correspondingly with the thickness of MCCP (controlled by print speed for MCCP dosage). (**J**) CPL and the corresponding luminescence dissymmetry factor spectra of different rotated CPL devices. (**K** and **L**) Emission intensity of the left- and right-handed devices as a function of polarization angle without (K) and with the quarter wavelength plate (L) in the polar coordinate system, where θ represents the transmission angle.

dihydrothieno-1,4-dioxin)–poly(styrene sulfonate) (PEDOT:PSS) electrodes (fig. S5), exhibiting adjustable multicolor electro-CPL (fig. S6).

Subsequently, these microdevices were integrated, and being a pixel-controllable CPL array, through the patterned spraying of orthogonal conductive circuits and the alternately covering of left- and right-handed MCCP (Fig. 3A). After the array encapsulation and combination with the crossbar configuration-based control system which demonstrated notable applicability in large-scale display, an adaptable stereoscopic display panel was obtained (Fig. 3B and fig. S7). We then analyzed the panel's relative deviation of electroluminescence intensity, and found that it was ca. 8% in 100-unit (fig. S8,

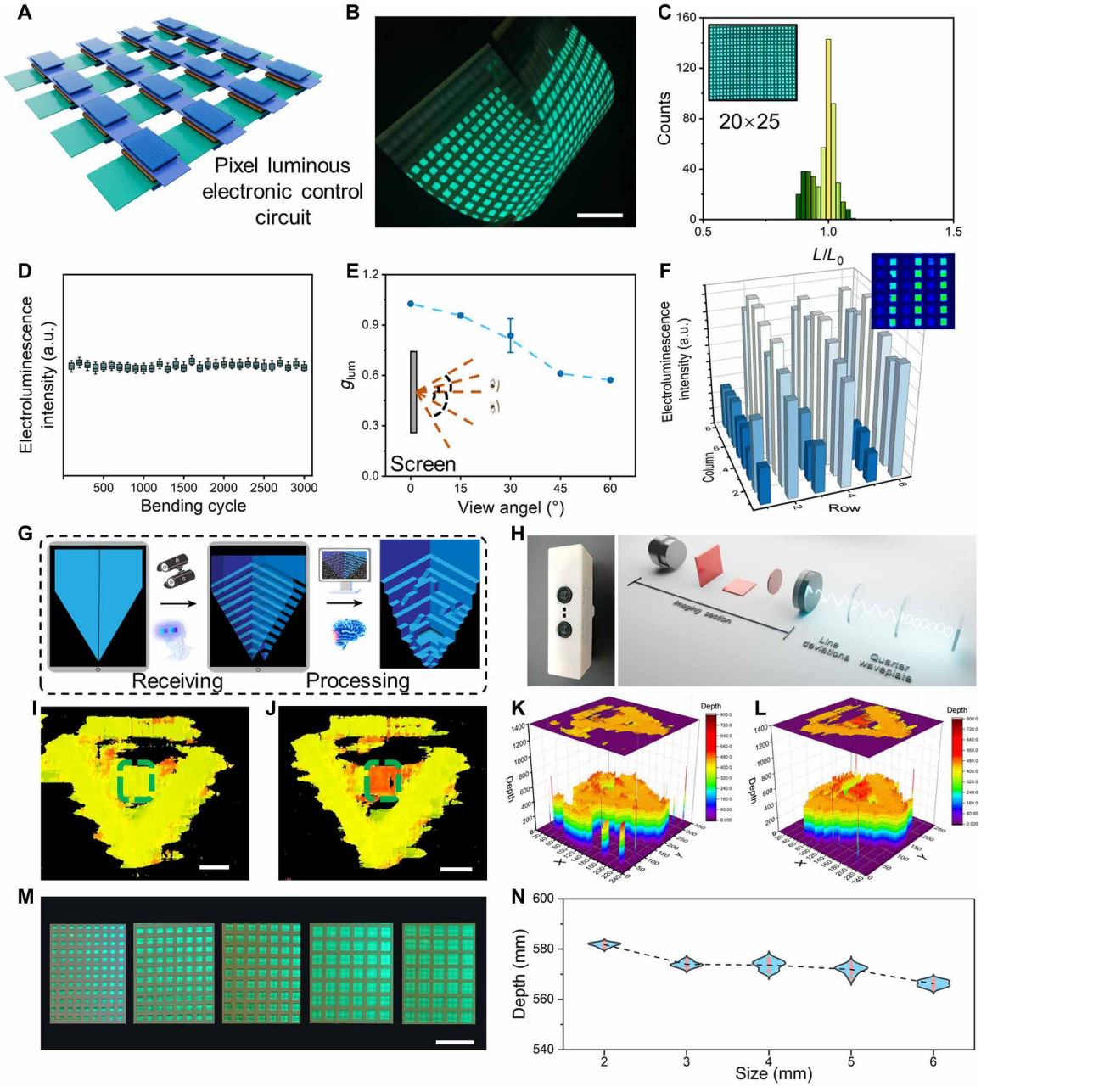

Fig. 3. CPL spatial panel performance. (**A**) Schematic of the integrated CPL panel. (**B**) Photograph of the bent CPL panel. Scale bar, 2 cm. (**C**) Statistical distribution of the relative deviation (luminance of one single unit minus the average value) in emission intensity for 500 CPL units, inset showing the working photograph. (**D**) Electro-CPL intensity of the bent CPL panel under bending cycling. (**E**) g_{lum} values at various view angles. (**F**) The CPL intensity distinction observed by polarizer when powering on display, and inset showing brightness-discrepancy map. (**G**) Conceptual illustration of the depth information acquisition mechanism. (**H**) Photograph and schematic of depth apparatus. (**I** to **L**) Depth images of the display collected by the depth apparatus before (I) and after (J) wearing CPL-functional glasses (dashed zone showing stereo-effect) at a measure distance of 60 cm, with the corresponding digital results in (K) and (L). Scale bars in (I) and (J), 3 cm. (**M**) Photograph of CPL panel with different pixel sizes. Scale bar, 2 cm. (**N**) The depth information corresponding to the display in (M), and the depth information generated by binocular stereo vision increase with the increase of pixel size.

A and B) and less than 15% in 500-unit (Fig. 3C) panels, respectively, which indicates the scalable production capacity towards further practice. The integrated display maintained stable electroluminescence intensities, the alterations below 5%, after 2000 switching cycles (fig. S8C) and over a 200-hour continuous operation (fig. S8D) under actual usage conditions, respectively. The suppleness of the electro-CPL panel enables the large-sized external force–driven arbitrary bending, while persisting high-performance electroluminescence and a viewing effect that meets commercialization requirement (Fig. 3D and fig. S8E). The strongly boosted electro-CPL by MCCP layer with satisfying g_{lum} values (fig. S8F) and remained almost constant with different driven voltage (fig. S8G) and continuous operation (fig. S8H). We also varied working environments, under some extreme conditions, and our 3D displaying device showed the durability (figs. S8I and S9). The AC-driven electroluminescent devices, constructed with emissive materials embedded in flexible and stretchable dielectric matrices, generally have higher requirements for operating voltage and energy supply but exhibit exceptional mechanical adaptability to deformation, making them ideal candidates for applications in flexible spatial displays and human-machine interactive sensory interfaces (figs. S10 and S11). With the large g_{lum} values (over 0.5) at various observing angles, adapting to its flexion or user movement (Fig. 3E), also led to the remarkable brightness discrepancy of the adaptable display under the polarizer (Fig. 3F).

The images with subtle differences of the same object are captured by two eyes separately and then processed by the brain to obtain depth information, that is, binocular stereo vision (*28*–*31*) (Fig. 3G). We then used a depth apparatus composed of two cameras (Fig. 3H) with the same eye distance as humans to quantify the stereoscopic imaging effect of the display mode (fig. S12, A and B), whose built-in algorithm could simulate the brain, calculating the depth information of the observed object with an accuracy exceeding 95% (fig. S12C). The as-measured depth information of the stereo imaging area on the CPL-pixel panel changed conspicuously with and without polarized glasses (Fig. 3, I and J and movie S3). We then calculated the actual depth information (Z, cm) with the formula as follows

$$Z = 8 \times 33{,}090.534 / D$$

D is the distance acquired by the cameras. The as-calculated depth of the stereoscopic image is approximately 5 cm in this case (Fig. 3, K and L, and fig. S12D), offering the chance for further precise control applications. This algorithm could also be extended to various pixel sizes (Fig. 3, M and N) for demonstrating substantial stereoscopic imaging effects.

The discrepant-handedness CPL panel comes on stream immediately for its most promising application, stereoscopic display. Furthermore, we have completed a large-sized bendable CPL stereoscopic panel containing over 1×10^4 neo-micro-CPL devices (Fig. 4A) and another small-sized panel with a pixels per inch reaching 85 (fig. S13).

The as-prepared CPL-pixel panel, working with designed smart polarized glasses (Fig. 4B), alternatively transmits left- and right-handed CPL and further connects to intelligent devices (fig. S14), to achieve immersive human-robot interaction. Building upon this, we conducted the human-robot interaction using our circularly polarized spatial displays, attaining an immersive experience of virtual world for users (Fig. 4C and movie S4).

Going one step further, we practiced the virtual reality interaction potential of the stereoscopic-imaging CPL-pixel panel and human-robot action synchronization device (Fig. 4D and fig. S15). When the user grasped the in-depth cube in the panel, the elsewhere robotic arm could perform the same operation for the actual object synchronously (Fig. 4E and movie S5). The system demonstrates over 90% accuracy in grasping objects at varying distances, ensuring its reliability in application (Fig. 4F).

We further expanded to real-world scenarios to showcase the potential in practice, for example, disaster relief, focusing on conditions prone to secondary disasters (e.g., earthquakes) that would endanger the safety of rescue personnel (Fig. 4, G and H). To better leverage the advantages of this stereoscopic display system, achieve more precise control over display effects, and enhance depth perception contrast with the surrounding environment, thereby facilitating real-time scene reconstruction and remote rescue operations, our depth information–based simulation for trapped personnel rescue scenarios represents human-shaped targets using rectangular regions (Fig. 4I). Benefiting from all the above optimization, we successfully operated the robot to remotely rescue trapped "personnel," ensuring the safety of rescue personnel to the most extent (Fig. 4, J to L, and movie S6).

DISCUSSION

In summary, we fabricate an adaptable spatial displaying enabled human-robot interaction system, mainly composed of the chiral conversion layer and the electroluminescent section to achieve highly-asymmetric electro-CPL. The left- and right-handed CPL pixels arrange alternately to form the arrays of the panel for founding immersive stereo imaging with intelligent polarized glasses. Development of this straightforward, stable, and highly operational display also encourages us to investigate neo-characterization to precisely capture the depth information and quantify the stereo imaging for further practice. With that, we showcase an immersive human-robot interaction and successfully simulate the ideal secure rescue in a disaster scenario, building the bridge between the real world and the digital universe.

MATERIALS AND METHODS

Materials and chemicals

The nematic liquid crystal host E7 (n = 1.747 and Tc = 60°C) and the chiral dopants R/S5011 were purchased from Shijiazhuang Yesheng Chemical Technology Co. Ltd. PEDOT:PSS (1.4% in water), PVA (99.5%), PAM, 2-hydroxy-2-methylpropiophenone (98%), *N*,*N*′-methylenebisacrylamide (99%), and acrylamide (99%) were purchased from Adamas. Ethyl alcohol and chloroform were purchased from Sinopharm Chemical Reagent Co. Ltd. ZnS phosphor and thermoplastic polyurethane were purchased from Xin Shuangjian Technology Co. Ltd. All chemicals were used directly without any further purification.

Synthesis of prepolymers for photopolymerization materials

We developed a method to prepare scalable prepolymers of PAM (*32*, *33*). First, 12.65-g acrylamide was dissolved in 100 ml of water, and then 1.80-g poly(acrylamide) was added. Subsequently, the solution was heated to 60°C at a rate of 10°C/min and stirred for 4 hours. After that, 0.20-g 2-hydroxy-2-methylpropiophenone and 0.20-g *N*,*N*′-methylenebisacrylamide were added, and the solution was continuously stirred for 2 hours in dark. After cooling to room temperature, it was stored in a dark environment for further use.

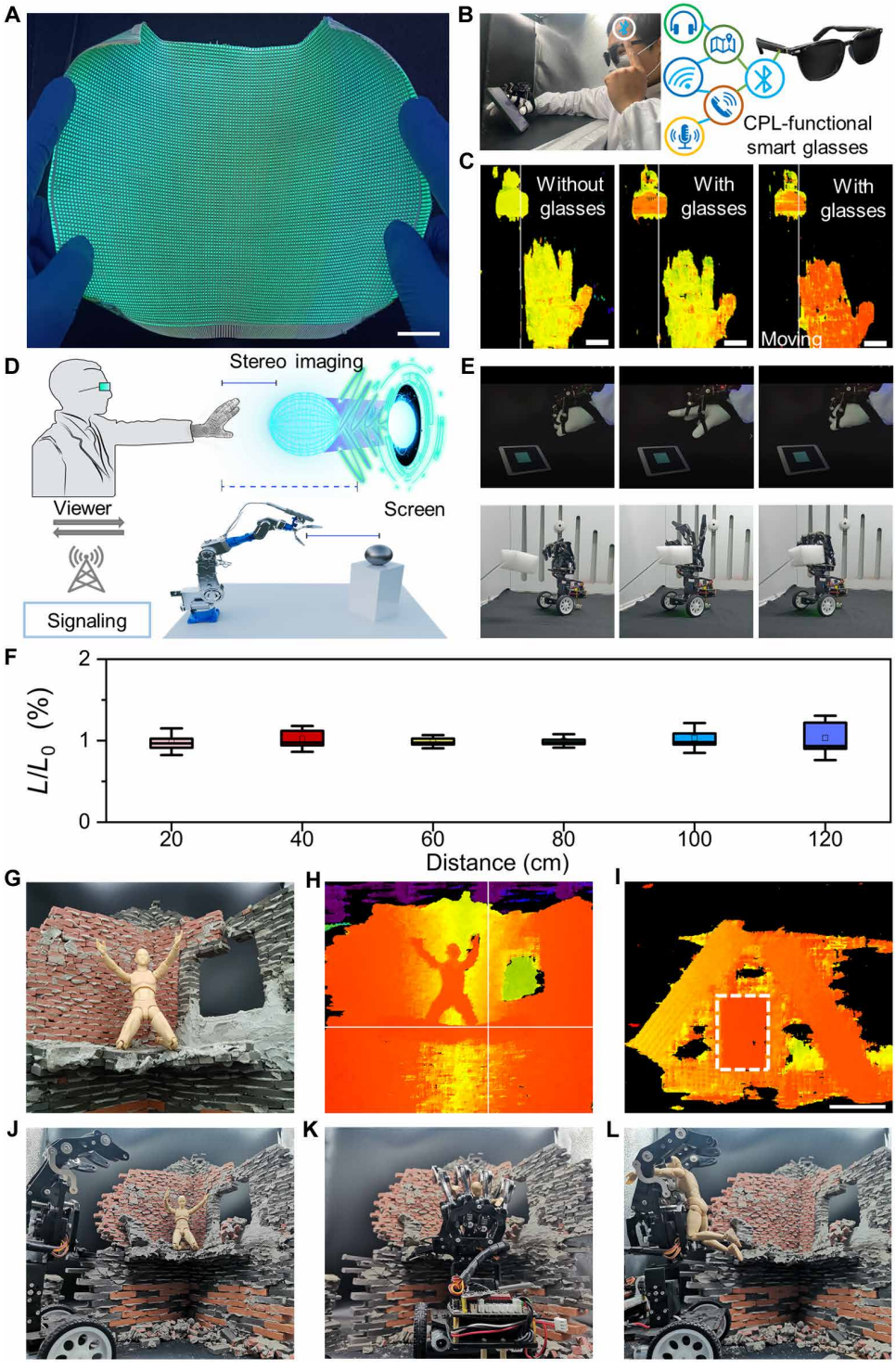

Fig. 4. Practice of CPL display-offered depth information. (**A**) Photograph of a large-sized bendable CPL spatial panel. Scale bar, 3 cm. (**B**) Photographs of the user wearing CPL-functional glasses, allowing for stereo vision and interaction with smart devices. (**C**) The depth information of the pattern in the display changes after wearing polarized glasses, which plays a role in human-robot interaction. Scale bars, 5 cm. (**D**) Schematic diagram of the stereo imaging enabled immersive remote human-robot interaction. (**E**) Photographs of the remote user-robot synchronous grasping action frames. (**F**) The accuracy of remote collaboration based on depth information. L_0 is the depth information of the panel measured by depth apparatus, and L is the one of the user's hand when grasping. (**G** and **H**) Photograph (G) and the actual depth image (H) of a "trapped individual." (**I**) The depth information of "trapped individual" (dashed area) in spatial display. Scale bar, 5 cm. (**J** to **L**) Photographs of the stereo-imaging enabled step-by-step disaster-relief practice.

Chiral liquid crystals fabrication

We prepared chiral liquid crystals (CLCs) with different PBGs by mixing E7 with chiral dopants R/S5011 (*34*, *35*). A series of chiral dopants with weight ratios of 2.28, 2.79, and 3.15 weight % (wt %) were introduced to obtain CLCs with PBG in the red, green, and blue regions, respectively. Nematic liquid crystals and chiral dopants were dispersed in chloroform with ultrasonic treatment for 5 min, and then the CLCs mixture was obtained after evaporating the solvent in a drying box for ca. 48 hours.

Synthesis of precursor multimicrosphere circular collaborative polarizer

To obtain CLCs microspheres with suitable size (*36*, *37*), we devised an aqueous one-pot synthesis method. We mixed 0.51 g of CLCs, 2.00 g of PVA solution (10 wt % in water), and 3.00 g of prepolymers for photopolymerization materials in the vial, and then used a high-speed emulsifier (IKAT18, Germany) to stir at 10,000 rpm for 5 min for achieving the evenly dispersed CLCs microspheres of the desired size.

Production of luminescent pixel points

We used spray coating to create the intended pattern on various substrates. Initially, the desired shape (width, 2 mm) of the lower electrode was achieved by combining masks, and then a substrate that matched the size was securely attached. Then, PEDOT:PSS (mixed with ethanol in a 1:3 weight ratio) was poured into the reservoir of an airbrush pen (S-130, Ningbo SIBONGD Electromechanical Technology Co. Ltd) powered by an air pump (AF18, Ningbo HSENG Pneumatic Machinery Co. Ltd) and spray coated onto the black substrate with 0.9 bar compressed air. We moved the airbrush pen back and forth until the substrate is evenly covered by PEDOT:PSS, and then dried it with hot air at 50°C for 2 min and repeat the above process three to four times. During the spraying process, we maintained a 15 cm distance between the airbrush pen and the substrate, with no specific humidity requirement. A blend of ZnS phosphor and thermoplastic polyurethane (weight ratio of ZnS, 45%) was evenly spread onto the lower electrode and then subjected to a 60°C oven for ca. 24 hours to achieve a consistent thin film. Subsequently, an orthogonal upper electrode was applied on top of the luminescent layer following the same procedure as the lower electrode, and luminescent pixel points formed at the intersections.

Production of real-time multilayer stereoscopic panel based on CPL

A pneumatic extrusion-type microelectronic printer (MP1100, Prtronic, China) was used for chiral layer printing. The uncured MCCP was loaded into a 5.0-ml syringe barrel with a nozzle having an inner diameter of 250 μm. The release of uncured MCCP was accurately regulated by adjusting the printing speed and pressure. Patterns are customizable through the drawing software provided by the printer. The uncured MCCP was printed evenly on the emitting part, and the overflow part gradually returned to the emitting part by the self-propelled capacity, reducing the printing accuracy requirements. The left- and right-handed uncured MCCPs were alternately printed into the surface of the electroluminescence section, respectively. Last, closely attached, fixed MCCP on the top surface of the electroluminescence section was created after being exposed to 365-nm UV light for 5 min.

Characterization

The UV-visible (UV-vis) near-infrared spectrophotometer (Shimadzu 3700 DUV) was used for transmission and UV-vis spectra, Hitachi F-4700 fluorescence spectrophotometer for fluorescence spectra. CD and CPL spectra were measured on a JASCO J-1500 and JASCO CPL-300 spectrophotometer, respectively. Polarized optical microscopy images were recorded on the material microscope upright at Mshot MP41. The Fourier transform infrared (FTIR) spectrum was measured with an FTIR microscope (Nicolet iN10MX). The TG-DSC curve and DSC curves were recorded on a thermogravimeter (TA Discovery TGA) and a differential scanning calorimeter (Shimadzu, DSC-60), respectively. SEM images were obtained by using a field-emission scanning electron microanalyzer (Zeiss Supra 40 scanning electron microscopes at an acceleration voltage of 1.5 kV). The circular polarization characteristic of emission of the display was demonstrated by converting CPL to linearly polarized light using a quarter-wave slice (350 to 850 nm, Thorlabs), and then the direction of linear polarization was discriminated by a rotating polarizer (400 to 700 nm, Thorlabs). Brightness intensity was performed on brightness meter (Hopoocolor, CX1000). Electro-optical conversion efficiency is measured by the comprehensive light-color-electricity test system (Hopoocolor, HPCS-6500) with an integrating sphere. The depth information was calculated by a homemade binocular depth apparatus (based on Xiangyuanyuedong, D405). The temperature information is measured and calculated by an infrared thermometer (DELIXI, DM5005).

Supplementary Materials

The PDF file includes:

Supplementary Text
Figs. S1 to S15
Legends for movies S1 to S6
Legend for data S1
References

Other Supplementary Material for this manuscript includes the following:

Movies S1 to S6
Data S1

REFERENCES AND NOTES

1. Y. Tan, H. Godaba, G. Chen, S. T. M. Tan, G. Wan, G. Li, P. M. Lee, Y. Cai, S. Li, R. F. Shepherd, J. S. Ho, B. C. K. Tee, A transparent, self-healing and high-κ dielectric for low-field-emission stretchable optoelectronics. *Nat. Mater.* **19**, 182–188 (2019).
2. X. Shi, Y. Zuo, P. Zhai, J. Shen, Y. Yang, Z. Gao, M. Liao, J. Wu, J. Wang, X. Xu, Q. Tong, B. Zhang, B. Wang, X. Sun, L. Zhang, Q. Pei, D. Jin, P. Chen, H. Peng, Large-area display textiles integrated with functional systems. *Nature* **591**, 240–245 (2021).
3. R. R. Bruno, N. Bruining, C. Jung, the VR-ICU Study group, Virtual reality in intensive care. *Intens. Care Med.* **48**, 1227–1229 (2022).
4. M. O. Ernst, M. S. Banks, Humans integrate visual and haptic information in a statistically optimal fashion. *Nature* **415**, 429–433 (2002).
5. D. Fattal, Z. Peng, T. Tran, S. Vo, M. Fiorentino, J. Brug, R. G. Beausoleil, A multi-directional backlight for a wide-angle, glasses-free three-dimensional display. *Nature* **495**, 348–351 (2013).
6. K. R. Pyun, J. A. Rogers, S. H. Ko, Materials and devices for immersive virtual reality. *Nat. Rev. Mater.* **7**, 841–843 (2022).
7. A. T. Lam, J. Ma, C. Barr, S. A. Lee, A. K. White, K. Yu, I. H. Riedel-Kruse, First-hand, immersive full-body experiences with living cells through interactive museum exhibits. *Nat. Biotechnol.* **37**, 1238–1241 (2019).
8. F. S. Hage, G. Radtke, D. M. Kepaptsoglou, M. Lazzeri, Q. M. Ramasse, Single-atom vibrational spectroscopy in the scanning transmission electron microscope. *Science* **367**, 1124–1127 (2020).
9. D. C. Schedl, I. Kurmi, O. Bimber, An autonomous drone for search and rescue in forests using airborne optical sectioning. *Sci. Robot.* **6**, eabg1188 (2021).
10. B. Li, Q. Lin, M. Li, Frquency-angular resolving LiDAR using chip-scale acousto-optic beam steering. *Nature* **620**, 316–322 (2023).

11. S. Romanick-Schmiedl, G. Raghu, Telemedicine-maintaining quality during times of transition. *Nat. Rev. Dis. Primers.* **6**, 45 (2020).
12. N. Davis, J. Heikenfeld, C. Milla, A. Javey, The challenges and promise of sweat sensing. *Nat. Biotechnol.* **42**, 860–871 (2024).
13. Y. Gao, S. Chien, Review on space robotics: Toward top-level science through space exploration. *Sci. Robot.* **2**, eaan5074 (2017).
14. R. Tahira, G. James, Inclusion in human-machine interactions. *Science* **375**, 149–150 (2022).
15. R. T. Scott, L. M. Sanders, E. L. Antonsen, J. J. A. Hastings, S.-m. Park, G. Mackintosh, R. J. Reynolds, A. L. Hoarfrost, A. Sawyer, C. S. Greene, B. S. Glicksberg, C. A. Theriot, D. C. Berrios, J. Miller, J. Babdor, R. Barker, S. E. Baranzini, A. Beheshti, S. Chalk, G. M. Delgado-Aparicio, M. Haendel, A. A. Hamid, P. Heller, D. Jamieson, K. J. Jarvis, J. Kalantari, K. Khezeli, S. V. Komarova, M. Komorowski, P. Kothiyal, A. Mahabal, U. Manor, H. G. Martin, C. E. Mason, M. Matar, G. I. Mias, J. G. Myers Jr., C. Nelson, J. Oribello, P. Parsons-Wingerter, R. K. Prabhu, A. A. Qutub, J. Rask, A. Saravia-Butler, S. Saria, N. K. Singh, M. Snyder, F. Soboczenski, K. Soman, D. Van Valen, K. Venkateswaran, L. Warren, L. Worthey, J. H. Yang, M. Zitnik, S. V. Costes, Biomonitoring and precision health in deep space supported by artificial intelligence. *Nat. Mach. Intell.* **5**, 196–207 (2023).
16. F. Wang, C. Wang, M. Chen, W. Gong, Y. Zhang, S. Han, G. Situ, Far-field super-resolution ghost imaging with a deep neural network constraint. *Light Sci. Appl.* **11**, 1 (2022).
17. M. Song, L. Feng, P. Huo, M. Liu, C. Huang, F. Yan, Y. Lu, T. Xu, Versatile full-colour nanopainting enabled by a pixelated plasmonic metasurface. *Nat. Nanotechnol.* **18**, 71–78 (2023).
18. F. Furlan, J. M. Moreno-Naranjo, N. Gasparini, S. Feldmann, J. Wade, M. J. Fuchter, Chiral materials and mechanisms for circularly polarized light-emitting diodes. *Nat. Photon.* **18**, 658–668 (2024).
19. Y. Zhou, Y. Wang, Y. Song, S. Zhao, M. Zhang, G. Li, Q. Guo, Z. Tong, Z. Li, S. Jin, H. B. Yao, M. Zhu, T. Zhuang, Helical-caging enables single-emitted large asymmetric full-color circularly polarized luminescence. *Nat. Commun.* **15**, 251 (2024).
20. J. Wang, H. Zhou, J. Yang, L. Feng, J. Yao, K. Song, M. Zhou, S. Jin, G. Zhang, H. B. Yao, Chiral phosphine-copper iodide hybrid cluster assemblies for circularly polarized luminescence. *J. Am. Chem. Soc.* **143**, 10860–10864 (2021).
21. M. Zhang, Q. Guo, Z. Li, Y. Zhou, S. Zhao, Z. Tong, Y. Wang, G. Li, S. Jin, M. Zhu, T. Zhuang, S. H. Yu, Processable circularly polarized luminescence material enables flexible stereoscopic 3D imaging. *Sci. Adv.* **9**, eadi9944 (2023).
22. P. Zhang, I. M. Lei, G. Chen, J. Lin, X. Chen, J. Zhang, C. Cai, X. Liang, J. Liu, Integrated 3D printing of flexible electroluminescent devices and soft robots. *Nat. Commun.* **13**, 4775 (2022).
23. C. Larson, B. Peele, S. Li, S. Robinson, M. Totaro, L. Beccai, B. Mazzolai, R. Shepherd, Highly stretchable electroluminescent skin for optical signaling and tactile sensing. *Science* **351**, 1071–1074 (2016).
24. W. C. Poh, A. L. S. Eh, W. Wu, X. Guo, P. S. Lee, Rapidly photocurable solid-state poly(ionic liquid) ionogels for thermally robust and flexible electrochromic devices. *Adv. Mater.* **34**, 2206952 (2022).
25. Y. Wu, M. Li, Z. Zheng, Z. Q. Yu, W. H. Zhu, Liquid crystal assembly for ultra-dissymmetric circularly polarized luminescence and beyond. *J. Am. Chem. Soc.* **145**, 12951–12966 (2023).
26. Q. Guo, M. Zhang, Z. Tong, S. Zhao, Y. Zhou, Y. Wang, S. Jin, J. Zhang, H. B. Yao, M. Zhu, T. Zhuang, Multimodal-responsive circularly polarized luminescence security materials. *J. Am. Chem. Soc.* **145**, 4246–4253 (2023).
27. M. L. Verge-Serandour, K. Alim, Active flows solve sudoku-like problems. *Nature* **627**, 39–40 (2024).
28. C. Rogers, A. Y. Piggott, D. J. Thomson, R. F. Wiser, I. E. Opris, S. A. Fortune, A. J. Compston, A. Gondarenko, F. Meng, X. Chen, G. T. Reed, R. Nicolaescu, A universal 3D imaging sensor on a silicon photonics platform. *Nature* **590**, 256–261 (2021).
29. X. Tian, R. Li, Z. Wang, J. Ma, High quality 3D reconstruction based on fusion of polarization imaging and binocular stereo vision. *Inform. Fusion* **77**, 19–28 (2022).
30. Y. Yan, Z. Li, L. Li, Z. Lou, Stereopsis-inspired 3D visual imaging system based on 2D ruddlesden-popper perovskite. *Small* **19**, e2300831 (2023).
31. L. Yi, B. Hou, H. Zhao, X. Liu, X-ray-to-visible light-field detection through pixelated colour conversion. *Nature* **618**, 281–286 (2023).
32. J. Zhang, Y. Hu, L. Zhang, J. Zhou, A. Lu, Transparent, ultra-stretching, tough, adhesive carboxyethyl chitin/polyacrylamide hydrogel toward high-performance soft electronics. *Nano. Micro. Lett.* **15**, 8 (2023).
33. A. Pantula, B. Datta, Y. Shi, M. Wang, J. Liu, S. Deng, N. J. Cowan, T. D. Nguyen, D. H. Gracias, Untethered unidirectionally crawling gels driven by asymmetry in contact forces. *Sci. Robot.* **7**, eadd2903 (2022).
34. H. K. Bisoyi, Q. Li, Liquid crystals: Versatile self-organized smart soft materials. *Chem. Rev.* **122**, 4887–4926 (2022).
35. J. Liang, W. Wen, F. Jin, Y. G. Rubo, T. C. H. Liew, R. Su, Polariton spin hall effect in a Rashba-Dresselhaus regime at room temperature. *Nat. Photon.* **18**, 357–362 (2024).
36. S. S. Lee, H. J. Seo, Y. H. Kim, S.-H. Kim, Structural color palettes of core-shell photonic ink capsules containing cholesteric liquid crystals. *Adv. Mater.* **29**, 1606894 (2017).
37. C. Yang, B. Wu, J. Ruan, P. Zhao, L. Chen, D. Chen, F. Ye, 3D-printed biomimetic systems with synergetic color and shape responses based on oblate cholesteric liquid crystal droplets. *Adv. Mater.* **33**, e2006361 (2021).
38. H. Wu, Y. Chen, W. Xu, C. Xin, T. Wu, W. Feng, H. Yu, C. Chen, S. Jiang, Y. Zhang, X. Wang, M. Duan, C. Zhang, S. Liu, D. Wang, Y. Hu, J. Li, E. Li, H. Wu, J. Chu, D. Wu, High-performance Marangoni hydrogel rotors with asymmetric porosity and drag reduction profile. *Nat. Commun.* **14**, 20 (2023).
39. C. Choi, J. Leem, M. Kim, A. Taqieddin, C. Cho, K. W. Cho, G. J. Lee, H. Seung, H. J. Bae, Y. M. Song, T. Hyeon, N. R. Aluru, S. Nam, D.-H. Kim, Curved neuromorphic image sensor array using a MoS_2-organic heterostructure inspired by the human visual recognition system. *Nat. Commun.* **11**, 5934 (2020).
40. F. Liao, Z. Zhou, B. J. Kim, J. Chen, J. Wang, T. Wan, Y. Zhou, A. T. Hoang, C. Wang, J. Kang, J. H. Ahn, Y. Cha, Bioinspired in-sensor visual adaptation for accurate perception. *Nat. Electron.* **5**, 84–91 (2022).

Acknowledgments

Funding: This work was supported by the National Key Research and Development Program of China grant 2021YFA1500400; National Natural Science Foundation of China grants 22071226, U1932213, 22271265, 22101270, 22471253, and 224B2116; Hundred Talent Program of the Chinese Academy of Sciences grant KJ2060007002; Collaborative Innovation Program of Hefei Science Center, Chinese Academy of Sciences grant 2022HSC-CIP016; Funding of University of Science and Technology of China grants KY2060000168, YD2060002013, KY2060000198, and KY2060000235; Anhui Provincial Natural Science Foundation grant BJ2060190120; National Key Research and Development Program of China grants 2018YFE0202201 and 2021YFA0715700; University Synergy Innovation Program of Anhui Province grant GXXT-2019-028; and New Cornerstone Investigator Program. **Author contributions:** Conceptualization: T.Z., S.-H.Y., Q.G., Z.L., Y.Z., and Z.T. Investigation: T.Z., Q.G., Z.L., Y.W., and M.Z. Methodology: T.Z., S.-H.Y., Q.G., and Y.Z. Resources: T.Z., S.-H.Y., Q.G., Z.L., and S.Z. Data curation: T.Z., S.-H.Y., Q.G., Z.L., and S.Z. Validation: T.Z., S.-H.Y., Q.G., Z.L., Y.Z., Y.W., G.L., and Z.T. Supervision: T.Z., S.-H.Y., Q.G., and Z.L. Formal analysis: T.Z., S.-H.Y., Q.G., Z.L., Y.W., and Z.T. Software: Q.G. Writing–original draft: T.Z., S.-H.Y., Q.G., Y.Z., and Y.W. Writing–review and editing: T.Z., S.-H.Y., Q.G., Z.L., S.Z., and G.L. Visualization: T.Z., S.-H.Y., Q.G., Z.L., Y.Z., Y.W., and Z.T. Project administration: T.Z., S.-H.Y., and Q.G. Funding acquisition: T.Z., S.-H.Y., and M.Z. **Competing interests:** The authors declare that they have no competing interests. **Data and materials availability:** All data needed to evaluate the conclusions in the paper are present in the paper and/or the Supplementary Materials.

Submitted 12 December 2024
Accepted 9 April 2025
Published 14 May 2025
10.1126/sciadv.adv2721